Article

Microstructure Evolution of a New Precipitation-Strengthened Fe–Al–Ni–Ti Alloy down to Atomic Scale

Flora Godor [1],[†], Martin Palm [2], Christian H. Liebscher [2], Frank Stein [2], Christoph Turk [1],[‡], Katharina Leitner [1],[‡], Boryana Rashkova [1],*** and Helmut Clemens [1]

[1] Department of Materials Science, Montanuniversität Leoben, Roseggerstr. 12, 8700 Leoben, Austria; flora.godor@voestalpine.com (F.G.); christoph.turk@bohler-edelstahl.at (C.T.); katharina.leitner@bohler-edelstahl.at (K.L.); helmut.clemens@unileoben.ac.at (H.C.)

[2] Max-Planck-Institut für Eisenforschung GmbH, Max-Planck-Str. 1, 40237 Düsseldorf, Germany; m.palm@mpie.de (M.P.); liebscher@mpie.de (C.H.L.); f.stein@mpie.de (F.S.)

* Correspondence: boryana.rashkova@unileoben.ac.at

[†] Present address: Voestalpine BÖHLER Aerospace GmbH & CO KG, Mariazellerstr. 25, 8605 Kapfenberg, Austria.

[‡] Present address: Voestalpine BÖHLER Edelstahl GmbH & CO KG, Mariazellerstr. 85, 8605 Kapfenberg, Austria.

Abstract: Ferritic materials consisting of a disordered matrix and a significant volume fraction of ordered intermetallic precipitates have recently gained attention due to their favorable properties regarding high-temperature applicability. Alloys strengthened by Heusler-type precipitates turned out to show promising properties at elevated temperatures, e.g., creep resistance. The present work aims at developing a fundamental understanding of the microstructure of an alloy with a nominal composition of 60Fe–20Al–10Ni–10Ti (in at. %). In order to determine the microstructural evolution, prevailing phases and corresponding phase transformation temperatures are investigated. Differential thermal analysis, high-temperature X-ray diffraction, and special heat treatments were performed. The final microstructures are characterized by means of scanning and transmission electron microscopy along with hardness measurements. Atom probe tomography conducted on alloys of selected heat-treated conditions allows for evaluating the chemical composition and spatial arrangement of the constituent phases. All investigated sample conditions showed microstructures consisting of two phases with crystal structures A2 and $L2_1$. The $L2_1$ precipitates grew within a continuous A2 matrix. Due to a rather small lattice mismatch, matrix–precipitate interfaces are either coherent or semicoherent depending on the cooling condition after heat treatment.

Keywords: ferritic alloys; microstructure; Heusler phases; X-ray diffraction (XRD); transmission electron microscopy (TEM); atom-probe tomography (APT)

1. Introduction

In the last few decades, Fe–Al-based alloys have been much investigated, with special focus on applicability at high temperatures. The Fe–Al–Cr–Ni system is of specific interest because these alloys show so-called coherent microstructures that consist of a disordered body-centered cubic (bcc) ferritic matrix (A2 structure) with ordered bcc-based NiAl precipitates (B2 structure) embedded therein [1–6].

However, one of the major drawback of these alloys is the poor creep resistance and their decline in strength above 700 °C [1,4,6,7] because of a rather low precipitate volume fraction and the unoptimized lattice mismatch between the matrix and precipitates. This misfit can be adjusted by alloying these materials with Ti, so that the Ni_2TiAl phase ($L2_1$ structure, Heusler phase) forms coherently within a continuous ferritic matrix [8,9]. These precipitates act as obstacles to dislocation motion, resulting in improved creep strength. Furthermore, Strutt et al. [10] showed that $L2_1$–Ni_2TiAl possesses better creep strength

than that of B2–NiAl; thus, it is even more effective in improving the high-temperature properties of alloys. A further advantage of these alloys is that a bcc-type equivalent to the coherent γ/γ' microstructure present in Ni-based superalloys can be produced because of the sufficiently small lattice mismatch between the $L2_1$ precipitates (a_0 = 0.5865 nm) and the A2 matrix ($2 \times a_0$ = 0.5732 nm) [11,12]. Fe-based superalloys are beneficial in comparison to Ni-based superalloys or austenitic steels due to their lower density, high thermal conductivity [1,2], low coefficient of thermal expansion, and reasonable material and comparably low production costs. Additionally, Fe–Al-based alloys exhibit good oxidation resistance. Due to their attractive properties, Fe–Al-based alloys are possible candidates for high-temperature applications, for example, in aerospace engines or power plants [13–16].

Recent studies [8,9,17–28] that were conducted on Fe–Al–Cr–Ni–Ti(–Mo) alloys found two distinct types of microstructures. On the one hand, the alloys can comprise a ferritic matrix and $L2_1$ precipitates. On the other hand, there is also the possibility that two-phase B2 + $L2_1$ precipitates form hierarchically within a ferritic matrix [8,9,17,19,21,26]. As Ti mainly partitions to the $L2_1$ phase, it enables the evolution of such hierarchical microstructures. Through variation in Ti concentration, the precipitation sequence can be adjusted [5,8,17,23,24]. Rawlings et al. [20] showed that Ti-containing alloys possess a secondary creep rate that is up to 4 orders of magnitude lower at a given stress than that for alloys without Ti.

The aim of the present study is to gain an indepth understanding of the microstructure of a novel precipitation-strengthened alloy based on Fe–Al–Ni–Ti. The present phases and their evolution are described for the first time for such a specific alloy composition. The idea behind this alloy is to reduce density through raising the Ti content to about 10 at. %, and eliminating Cr and Mo, in contrast to the above-mentioned Fe–Al–Cr–Ni–Ti(–Mo) alloys. At the same time, higher Ti content gives the possibility to generate a higher volume fraction of coherent Heusler precipitates. Fe and Ni occupy equal lattice positions within the quaternary $Fe_{2-x}Ni_xTiAl$ Heusler phase because of their similar atomic radii [28]. Therefore, the microstructural properties of this alloy were pre-estimated from ternary system Fe-Al-Ti.

Morphological characteristics such as the size, shape, and arrangement of the precipitates, and the evolution of the microstructure, especially the thermal stability of the phases, are analyzed in detail. For reproducing the γ/γ' microstructure of a Ni-based superalloy, generating a coherent microstructure is inevitable. In ternary system Fe–Al–Ti, a miscibility gap (A2 + $L2_1$) exists in which coherent microstructures can be formed [29]. However, for the present alloy composition, it is not known if it is possible to generate a coherent microstructure consisting of the two phases A2 and $L2_1$. Therefore, special emphasis was laid on the investigation of the matrix–precipitate interfaces in different heat-treated conditions. In addition, differences to the previously investigated Fe–Al–Cr–Ni–Ti alloys, which contained about 8 at. % Cr and 0, 2, 4 or 6 at. % Ti, were identified [8,9,17,19,20,23]. The microstructures after different heat treatments were, therefore, characterized employing scanning electron microscopy (SEM), transmission electron microscopy (TEM) and atom probe tomography (APT), along with Vickers hardness measurements in order to gain sound knowledge of the microstructure. Moreover, the phase-transition temperatures were determined with differential thermal analysis (DTA), and complementary high-temperature X-ray diffraction (HT-XRD) experiments were performed.

2. Materials and Methods

2.1. Material and Processing

In the present work, a ferritic alloy with a nominal composition of 60Fe–20Al–10Ni–10Ti (in at. %) was examined. An ingot of about 500 g was produced by high-frequency remelting (machine type: Lifumat Met. 3.3 from Linn High Therm, Hirschbach, Germany) and spin casting into a copper mold at the Chair of Ferrous Metallurgy, Montanuniversität Leoben, Austria. For the production of the alloy, technically pure raw materials were used

(Fe: 99.7 m.% and Al, Ni, Ti: 99.99 m.%). Chemical analysis was conducted by means of X-ray fluorescence spectroscopy. In Table 1, the measured chemical composition is compared with the nominal composition.

Table 1. Nominal and measured chemical compositions of the alloy in the as-cast state given in at. %. The chemical composition was analyzed by means of X-ray fluorescence spectroscopy.

	Fe	Al	Ni	Ti	Others
Nominal	Bal.	20	10	10	
Actual	Bal.	20.9	9.7	9.6	0.36

For the following investigations, specimens with dimensions of approximately $10 \times 10 \times 15$ mm^3 were machined. Homogenization treatments were performed in a high-temperature chamber furnace RHF 1600 from Carbolite at 1200 °C for 24 h followed by either water quenching or furnace cooling. Analyzing the water-quenched state enables a description of the microstructure present at 1200 °C. In binary Fe–Al alloys, the disorder/order transition from A2 to B2 or further ordering from B2 to D0$_3$ cannot be suppressed by water quenching [30]. Through a comparison of this specimen with the slowly cooled condition, the evolution of the microstructure during the cooling process can be investigated. To test the long-term stability of the microstructure at different temperatures, which could be interesting for technical applications, heat treatments were also performed at 900 °C for 100 h followed by water quenching and furnace cooling.

2.2. Experimental Techniques

In order to determine phase transitions, and solidus and liquidus temperatures, DTA was performed in a Setaram Setsys 1750 (France). All transition temperatures were determined from heating curves with heating rates of 10 and 20 K/min. The measurements were performed in alumina crucibles with a sample mass of about 120 mg.

HT-XRD experiments were conducted in Bragg–Brentano arrangement from room temperature up to 1050 °C in a Seifert ID3003 diffractometer (Germany)equipped with an Anton Paar (Austria) DHS 1100 high-temperature chamber using Co–K$_\alpha$ radiation.

Metallographic preparation of all specimens was performed using conventional techniques, which were also established for other Fe-based alloys (grinding and polishing to 1 µm with a diamond polishing solution). The microstructures in the as-cast and in the heat-treated state were analyzed by means of SEM employing a Zeiss EVO 50 (Germany). Images were taken in back-scattered electron (BSE) mode at an acceleration voltage of 10 kV.

TEM studies were conducted on a JEOL JEM-2200FS (Japan) operated at 200 kV and on a Philips CM12 (The Netherlands) operated at 120 kV. The JEOL JEM-2200FS was used for imaging in TEM and scanning TEM (STEM) mode, and for energy-dispersive X-ray spectroscopy (EDS) mappings and energy-filtered TEM (EFTEM) measurements. Selected area diffraction patterns (SADP) were taken on the Philips CM12. Thin foils for TEM investigations [31] and needle-shaped APT specimens [32] were prepared by a standard liftout technique employing a focused ion beam (FIB) workstation Versa 3D DualBeam from FEI (The Netherlands). After the liftout, TEM specimens were mounted on Cu grids.

APT measurements were performed using a Cameca local electrode atom probe (LEAP^{TM}) 3000X HR (France). Experiments were run in voltage mode for the determination of the phase compositions, and in laser mode to map larger regions of the specimens. In voltage mode, measurements were conducted at a temperature of 60 K with a pulse rate of 200 kHz, a pulse fraction of 20%, and a target evaporation rate of 1%. In laser mode, investigations were performed at 60 K with a pulse rate of 250 kHz a pulse energy of 0.3 nJ and a target evaporation rate of 0.5%. The detection efficiency for the laser and voltage modes was 37%. The reconstructions and the quantitative analysis of the phases were performed using software package Cameca IVAS^{TM} 3.6.8. (France)

Hardness measurements (Vickers HV10) were performed using universal testing machine M4C 025 G3M from Emco-Test (Austria). The given hardness values were calculated from the arithmetic mean of five indents.

3. Results and Discussion

3.1. XRD, DTA and High-Temperature XRD Experiments

At room temperature (RT), the alloy consists of two phases, i.e., disordered A2 and ordered $L2_1$, as shown in the XRD spectrum displayed in Figure 1. $L2_1$ ordering was identified by the presence of the superlattice reflections, e.g., (311), and the structures of both phases were confirmed by TEM investigations (see next section). The approximate lattice parameters were 0.288 nm (A2) and 0.581 nm ($L2_1$) (Table 2).
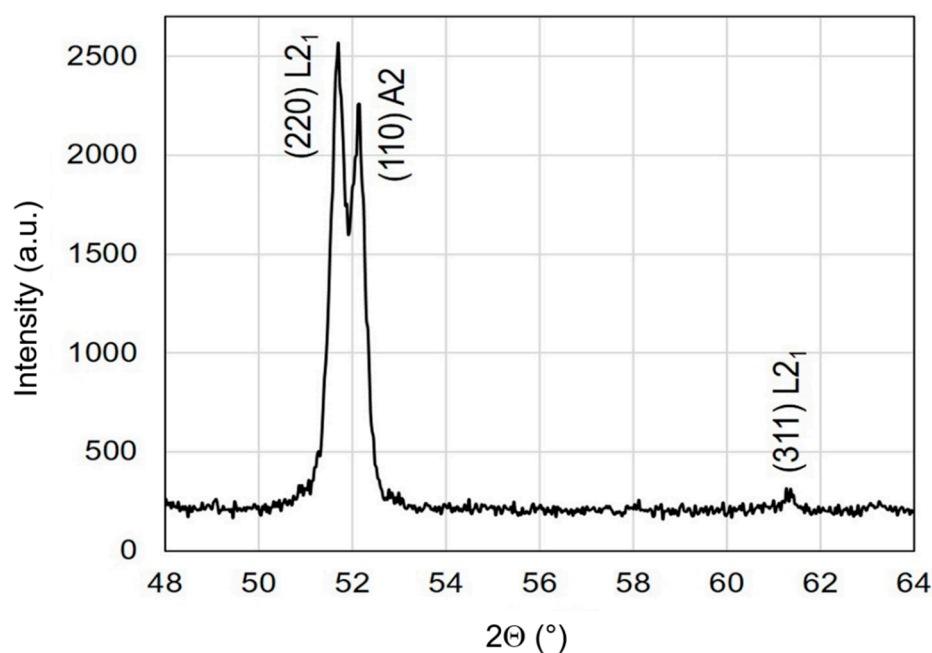

Figure 1. Section of XRD pattern of Fe–20.9Al–9.7Ni–9.6Ti measured at room temperature showing the two strongest peaks of A2 (110) and $L2_1$ (220), and the (311) superlattice reflection of $L2_1$.

Table 2. Lattice parameters (nm) and the calculated lattice mismatch Δ (%) of the A2 and $L2_1$ phases as determined by means of HT-XRD at room temperature (RT), and 900 and 1050 °C.

Phase	RT (nm)	900 °C (nm)	1050 °C (nm)
A2	0.2879	0.2915	0.2936
L21	0.5810	0.5899	-
Δ	0.9%	1.2%	-

In order to analyze the evolution of the phases in dependence on temperature, and particularly the phase-transition temperatures, DTA measurements were performed with complementary HT-XRD measurements. The DTA heating curve in Figure 2 shows a sharp peak at 720 °C associated with the Curie temperature, above which the alloy is no longer ferromagnetic, a broad signal in the range of about 920–1020 °C, the onset of melting (solidus) at 1291 °C, and the end of melting (liquidus) at 1355 °C.
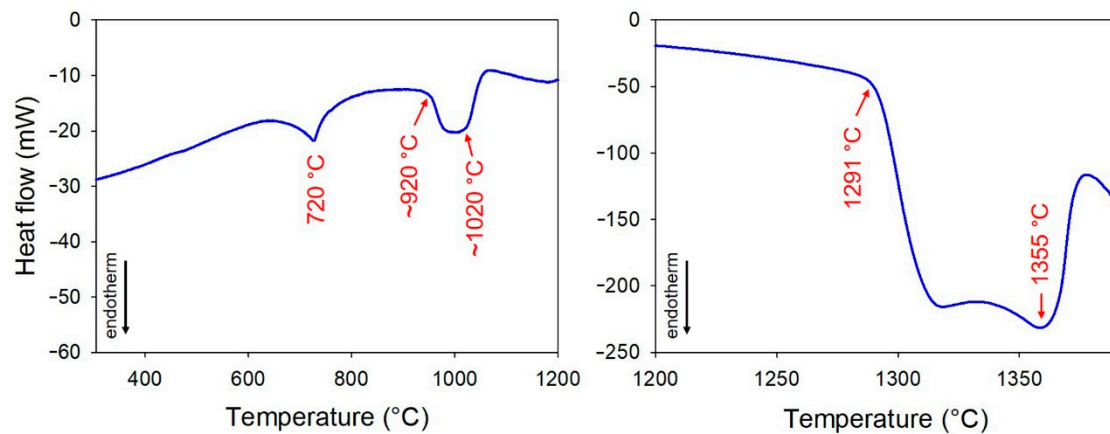
Figure 2. DTA heating curve of Fe–20.9Al–9.7Ni–9.6Ti determined with a heating rate of 20 K/min. For better visibility of the solid-state phase transformations, the curve was split into two parts, and the heat flow in the low-temperature part is shown in higher magnification.

In order to identify the phase transformation that yielded the broad signal between 920 and 1020 °C, an additional HT-XRD experiment was performed using the specimen that had been annealed at 900 °C for 100 h and subsequently furnace-cooled. Upon reheating to 900 °C, two distinct peaks were visible between 2θ angles of 50° and 52°, and the $(311)_{L2_1}$ peak was still visible, confirming the presence of A2 and $L2_1$ at that temperature (Figure 3). At 1050 °C, the two peaks between 2θ angles of 50° and 52° merged, and the $(311)_{L2_1}$ peak vanished, indicating the presence of a single-phase field region at this temperature. A thin Al_2O_3 layer was formed on the surface of the sample, resulting in additional peaks. After cooling to 900 °C, the same peaks were observed as after heating to 900 °C, i.e., A2 and $L2_1$ were present again. The lattice mismatch between these two phases increased slightly during heating from 0.9% at room temperature to 1.2% at 900 °C (Table 2).

Though the HT-XRD observations confirmed the DTA results that the alloy consisted of the two phases A2 and $L2_1$ up to 920 °C, it is not clear what happens above this temperature. The marked onset of the DTA signal at 920 °C (Figure 2) hints at the occurrence of a phase transformation, possibly $L2_1 \longleftrightarrow B2$. This could be followed by a rapid closing of the A2 + B2 miscibility gap, which could yield a continuous signal up to about 1020 °C. In view of the knowledge about phase equilibria in the Fe–Al–Ti system, such a scenario could be possible [33]. Above about 1020 °C, the alloy should be single-phase, most likely consisting of a disordered A2 phase.

3.2. Microstructural Investigations

Figure 4 shows SEM images of the microstructures in the as-cast state and after homogenization in the A2 single-phase field region at 1200 °C for 24 h and subsequent water quenching or furnace cooling. In the as-cast (Figure 4a) and in the homogenized state after water quenching (Figure 4b), no microstructural details could be resolved in the SEM. However, in the furnace-cooled state, dark precipitates could be seen that were embedded in a bright matrix phase (Figure 4c). Measurements of the compositions by EDS suggest that the matrix is the A2 phase and the precipitates were $L2_1$, which was later confirmed by the TEM results. $L2_1$ precipitates appeared to be regularly arranged along certain crystallographic orientations (Figure 4c). Furthermore, this image shows elongated particles that exhibited a brighter contrast in BSE mode. White arrows in the insert of Figure 4c exemplarily highlight some of these lines.
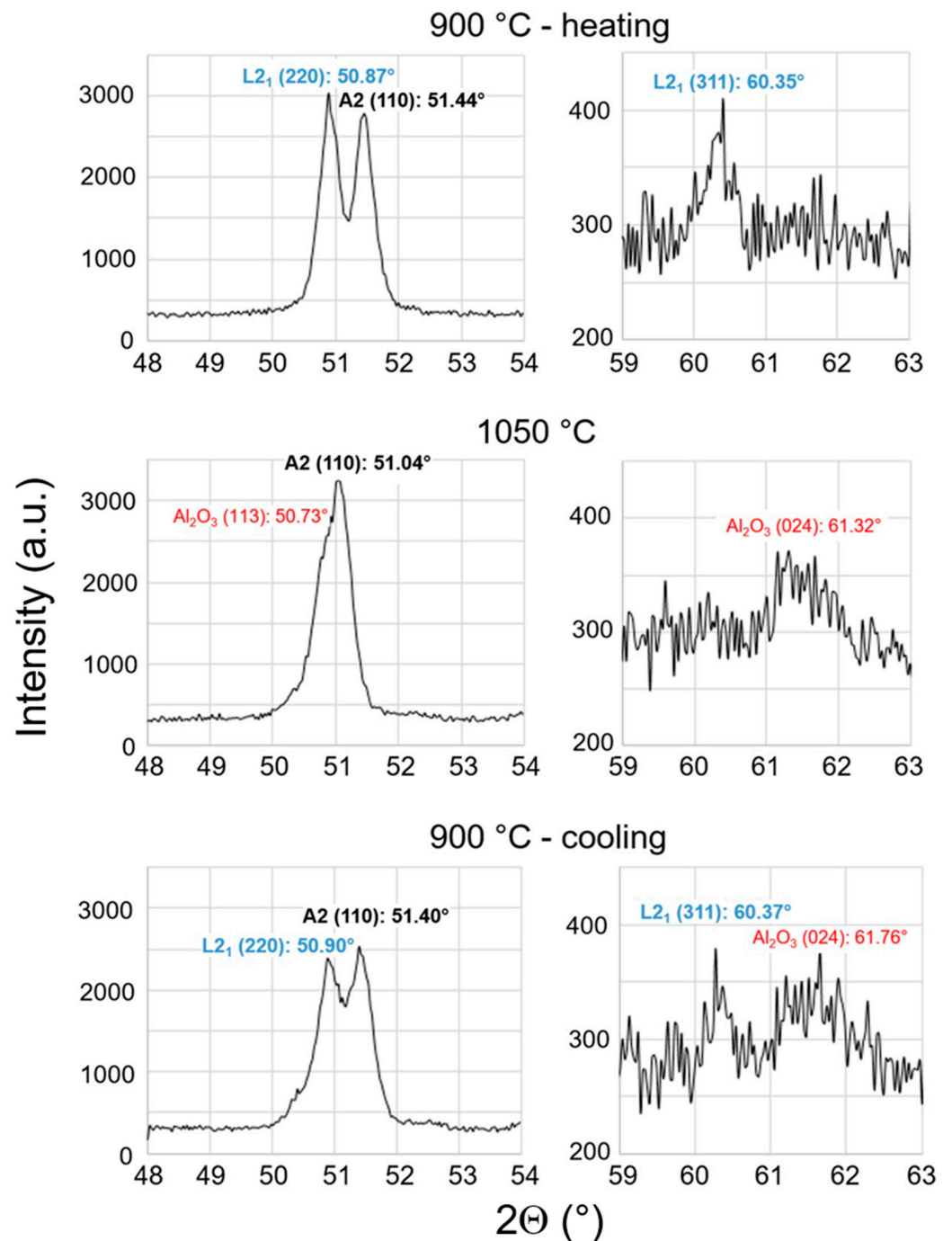
Figure 3. XRD patterns of Fe–20.9Al–9.7Ni–9.6Ti at 900 °C on heating, at 1050 °C on heating and at 900 °C on cooling showing the two strongest peaks of A2 (110) and L2$_1$ (220) and the (311) peak of L2$_1$. Above 950 °C, some Al$_2$O$_3$ formed on the surface of the sample, yielding additional peaks.

Results of the TEM measurements of the samples annealed at 1200 °C for 24 h in the single-phase field region are now discussed; in contrast to the as-cast state, they were cooled under controlled conditions. In Figure 5, bright-field (BF) STEM images are presented. Employing TEM the microstructure of the water-quenched state could be resolved (Figure 5a). It consisted of the two phases arranged in a mazelike way. In the slowly cooled state (Figure 5b), the microstructure also consisted of two phases, A2 and L2$_1$, with increased precipitate sizes in the range of about 300–700 nm.
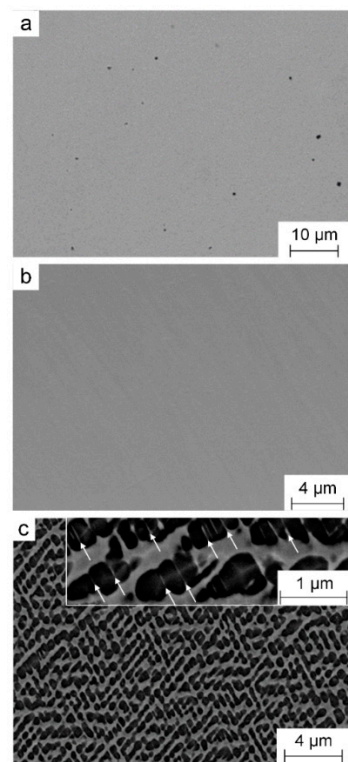
Figure 4. SEM images in BSE mode showing microstructures of (**a**) as-cast state and after heat treatment at 1200 °C for 24 h, followed by (**b**) water quenching and (**c**) furnace cooling. Black dots in (**a**) are defects resulting from metallographic preparation. In BSE mode, ferritic matrix (A2) exhibited a bright contrast, whereas L2$_1$ precipitates were dark. In the magnified insert in (**c**), arrows exemplarily denote elongated particles within the A2 phase.
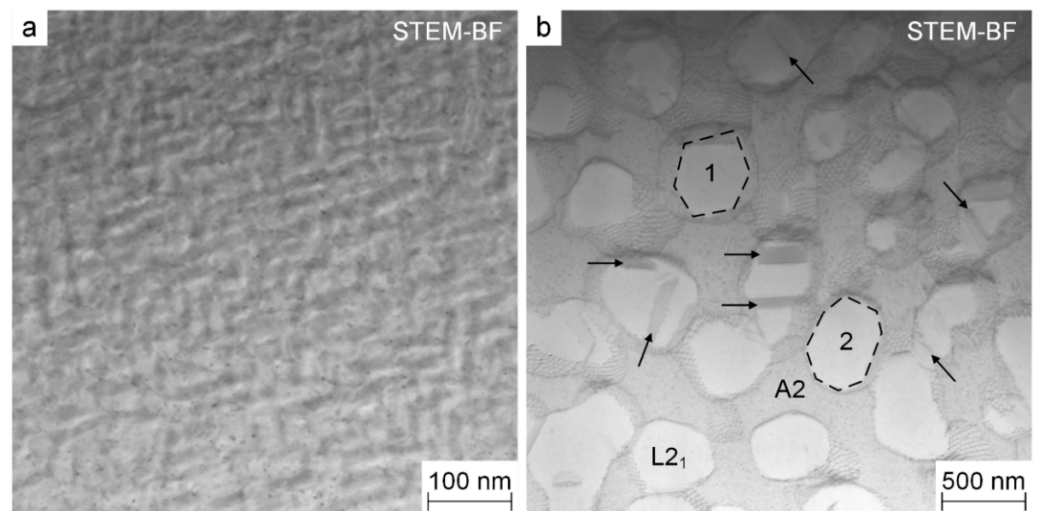

Figure 5. STEM-BF images after homogenization treatment at 1200 °C for 24 h followed by (**a**) water quenching or (**b**) furnace cooling. In the furnace-cooled condition, arrows highlight similar Fe-rich zones, as shown in Figure 4c. Furthermore, broken lines mark some polygonal L2$_1$ precipitates.

Comparing these two investigated states suggests that precipitate coarsening happens during furnace cooling. The morphology of the microstructure also changes, i.e., after rapid cooling the precipitates form elongated rods with high aspect ratios, whereas after slow cooling, they become spherical or rather polygonal (aspect ratio ≈ 1). As an example, one hexagonal particle (denoted with 1) and one octagonal particle (denoted with 2) are

shown in Figure 5b, where the precipitate ribbons with a darker contrast than that of the precipitates are highlighted by arrows. The arrows reveal that the ribbons were oriented along certain directions. Liebscher et al. [8], and Song et al. [9] reported similar findings within $L2_1$–Ni_2TiAl precipitates. They showed that these features correspond to antiphase boundaries (APBs), formed by a B2 or A2 phase depending on the Ti content of the alloy. In general, there are two different ways in which APBs can form within the $L2_1$ precipitates in this material. They are either created by the coalescence of two adjacent $L2_1$ precipitates [34,35] or they form by thermally induced order–disorder transitions within the precipitates [36]. In the present case, the APBs mainly developed through the coalescence of two ordered $L2_1$ particles that were out of lattice registry.

Exemplary results of the TEM investigation of a sample after thermal exposure at 1200 °C for 24 h and subsequent furnace cooling are shown in Figure 6, providing essential information on the formation of the microstructure. The selected area diffraction patterns (SADP), which were recorded along the [011] zone axis for both phases, verify that $L2_1$ precipitates were embedded in an A2 matrix (Figure 6b,c). The basic reflections are common to both phases ($[01\bar{1}]_{A2}$ corresponds to $[02\bar{2}]_{L21}$). As the $L2_1$ phase is an ordered Heusler phase, it can only be identified unambiguously in the <011> zone axis because of its characteristic <111> and <311> superlattice reflections [17].
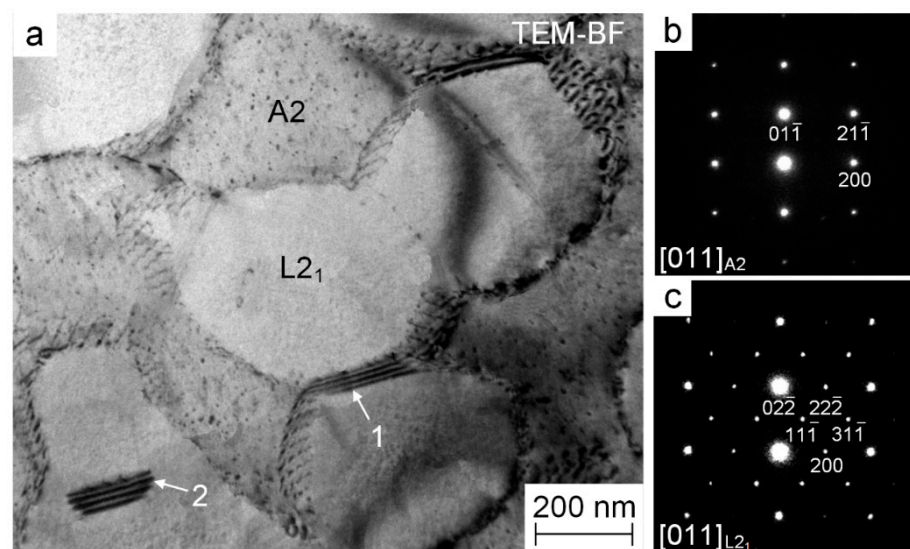
Figure 6. (**a**) TEM-BF image of a sample after thermal exposure at 1200 °C for 24 h and subsequent furnace cooling. Regions with a contrast arising from APBs are marked with "1" and "2". The black dots within the A2 phase are preparation artefacts. SADPs of (**b**) the matrix (A2 structure) and (**c**) the precipitates ($L2_1$ structure), acquired along the [011] axis.

Figure 6a shows two stages of coalescence (marked with "1" and "2") of the $L2_1$ precipitates. In "1" two particles were approached. As two ordered regions grew together, an APB was formed. This is in good accordance with the observations reported by Liebscher et al. [8], and Song et al. [19]. The confined APB ("2"), that was viewed under an inclination within the precipitate was formed by an overgrowth of the precipitate where the two ends of the APB unzip from the A2/$L2_1$ interface, leading to a constrained APB within two partial dislocations.

Figure 6a also shows that the precipitates were surrounded by a dense dislocation network. The lattice mismatch between matrix and particles was too large; thus, the elastic strain energy was relaxed by the formation of a dense misfit dislocation network at the phase boundaries, resulting in a semicoherent matrix–precipitate interface.

The elastic interaction energy between precipitates is attractive for long separation distances and repulsive for short ones, as described in [37–39]. The latter contributes to

the regular arrangement of precipitates, and repulsive forces prevent the precipitates from coalescing. In the present case, some of the precipitates impinged on each other under the formation of larger, elongated particles (Figure 6a). During furnace cooling, there was enough time for the $L2_1$ particles to coarsen, which is associated with an increase in the lattice misfit and hence the formation of an interfacial dislocation network. The relaxation of misfit strains does not provide sufficient elastic energy needed to maintain the alignment of the precipitates as reported in [37]. Hence, the precipitates adopted a more irregular shape and coalesced.

The TEM-DF image of the sample after thermal exposure at 1200 °C for 24 h and subsequent water quenching, see Figure 7a, was acquired using the (111) superlattice reflection, which is characteristic for the $L2_1$ phase. In the water-quenched state, precipitates could be assigned to the ordered $L2_1$ phase. As no dislocation network was found along the matrix–precipitate interface, it could be assumed that the precipitates were coherent with the A2 matrix. There was also a distinct difference in the phase compositions, as emphasized using EFTEM. In Figure 7b the Ti-rich precipitates appear bright, whereas the matrix appears dark. Combining DF imaging with EFTEM showed that the water-quenched microstructure consisted of an A2 matrix and nanoscale $L2_1$ precipitates.
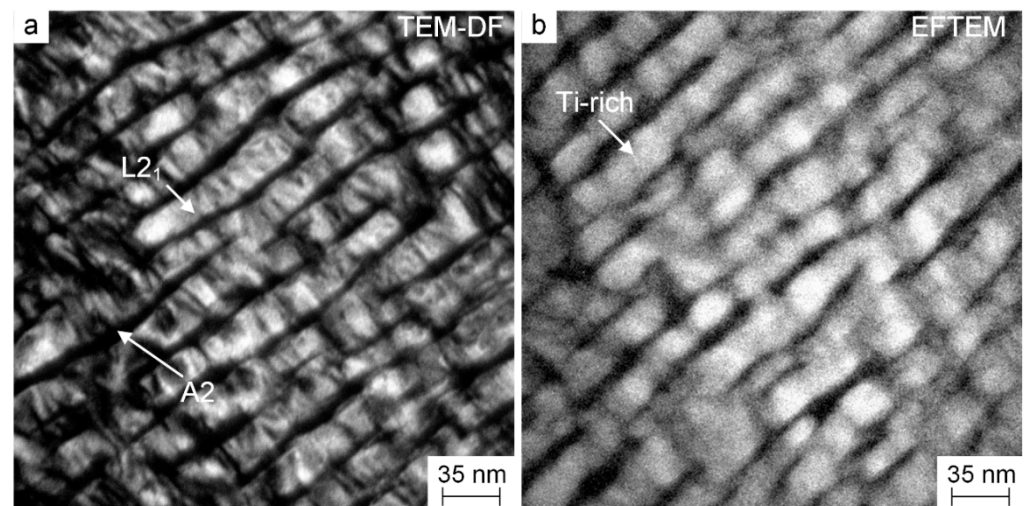
Figure 7. TEM investigation of a sample after thermal exposure at 1200 °C for 24 h and subsequent water quenching: (**a**) TEM-DF image taken using the (111) superlattice reflection, which is unique to the $L2_1$ crystal lattice and thus appears bright in contrast; (**b**) Ti map obtained by EFTEM indicating that there is a distinct difference in the Ti concentration of the two phases. (**a**,**b**) Different areas of the sample.

These techniques were also applied to the furnace-cooled state, as shown in Figure 8. Again, the DF image in Figure 8d was acquired with the (111) superlattice reflection. It is evident from the EDS mappings in Figure 8b,c that regions inside the precipitates that had been denominated as APBs were enriched in Fe, and depleted in Ti, Al and Ni. This is in accordance with the observations from the SEM shown in the insert of Figure 4c, where regions enriched in heavy elements, identified by their bright contrast in BSE mode, are exemplarily marked with arrows. Figure 8e shows the Fe map obtained from EFTEM analysis, which shows four $L2_1$ precipitates (dark contrast) that coalesced and formed APBs along their contact line. Each of the three resulting APBs showed enrichment in Fe.
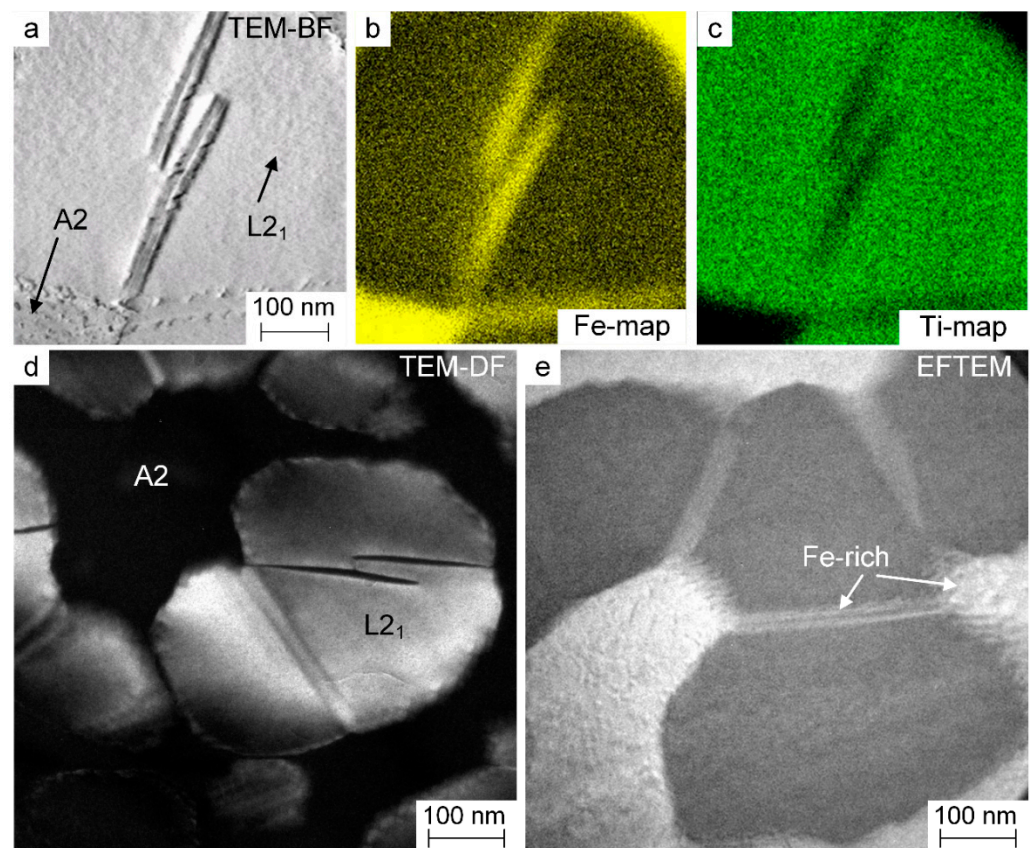
Figure 8. TEM investigation of sample annealed at 1200 °C for 24 h in the furnace-cooled state: (**a**) area where STEM-EDS mappings were performed; (**b**) Fe map representing ferritic matrix and (**c**) Ti map representing $L2_1$ precipitates; (**d**) TEM-DF image taken using the (111) superlattice reflection, which is unique to the $L2_1$ phase and thus this phase appears bright. The APBs can be seen, which appear in a dark contrast within the precipitates; (**e**) Fe map received from EFTEM analysis, proving that the APBs are enriched with Fe. (**d**,**e**) Different areas of the sample.

3.3. APT Measurements

In order to determine the chemical compositions of the nanometer-sized phases and to map selected regions, APT measurements were conducted on the samples that had been water-quenched or furnace-cooled from 1200 °C. In the reconstruction of the water-quenched specimen (Figure 9a), the phase boundary between precipitate and matrix is given by the isoconcentration surface at 55 at. % Fe colored in pink. $L2_1$ precipitates that had a lower Fe content are green. APT shows that the ferritic matrix is continuous. The precipitates form cuboids with aspect ratios >>1 (length of the shorter edge approximately 20–30 nm), which are separated by narrow channels of A2 phase.

After furnace cooling (Figure 9b), the precipitates were coarser (approximately 300–700 nm, see Section 3.2). In this reconstruction, isoconcentration surfaces at 48 at. % Fe are visualized in pink. The $L2_1$ precipitate that had a higher Ti content is represented by Ti atoms colored in green. A special microstructural feature that can just be resolved in the APT is the secondary precipitates in the center of the primary $L2_1$ precipitate. The isoconcentration surfaces indicate that these were Fe-rich particles that were solely present in the center of the $L2_1$ precipitate. In the outer part, i.e., in the vicinity of the matrix–precipitate interface, there was a subprecipitation free zone (SPFZ) of 40–50 nm where no Fe-rich particles existed. As these type of precipitates are solely present in the furnace-cooled state, but not in the water-quenched state, it can be concluded that they formed during the slow cooling process. The composition of $L2_1$ in equilibrium with A2 shifts to lower Fe contents with decreasing temperature, whereby $L2_1$ becomes oversaturated in Fe. This leads to

the formation of Fe-rich precipitates within the $L2_1$ precipitates with an SPFZ, where the diffusion paths are still short enough for the Fe atoms to reach the $A2/L2_1$ phase boundary. The fact that the composition of the $L2_1$ phase in equilibrium with A2 shifts towards Fe leaner compositions with decreasing temperature in the present Fe–Al–Ni–Ti alloy is in line with the corresponding shift of the $A2 + L2_1$ phase field in the Fe–Al–Ti system with decreasing temperature.
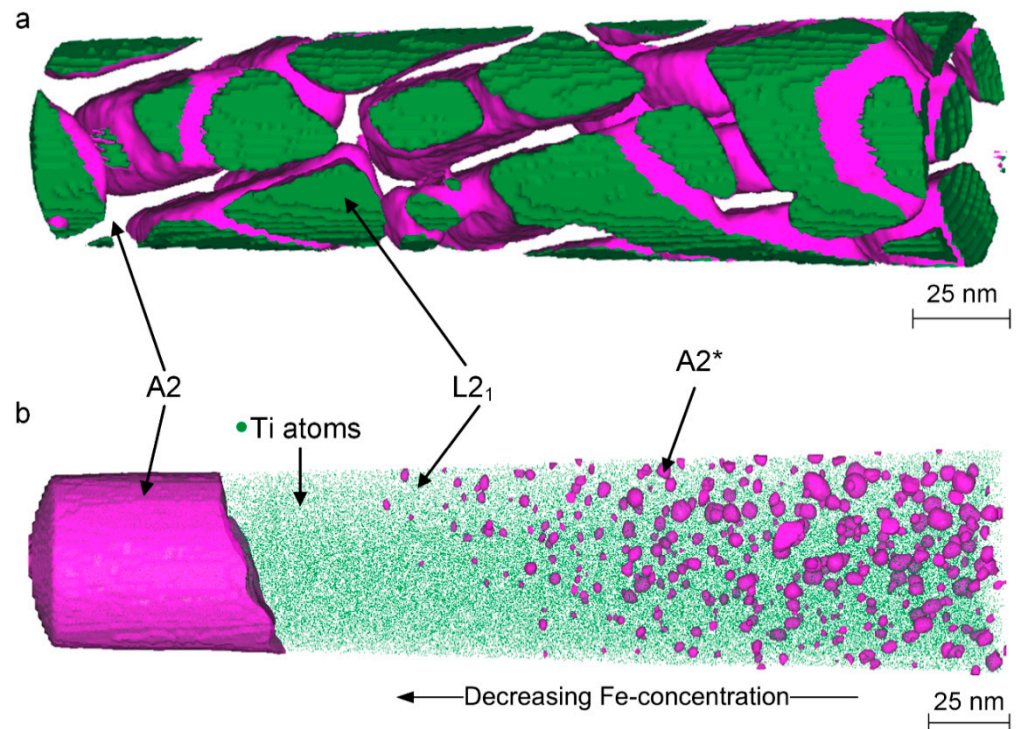
Figure 9. APT reconstructions of the sample after homogenization at 1200 °C for 24 h and subsequent (**a**) water quenching or (**b**) furnace cooling. Data were obtained from measurements conducted in laser mode (see text). (**a**) Pink surfaces correspond to isoconcentration surfaces at 55 at. % Fe. The interior of the particles is colored in green. The matrix phase was omitted here. (**b**) Isoconcentration surfaces at 48 at.% Fe are delineated in pink, marking the position of the Fe-rich A2 phase. The primary $L2_1$ precipitate can be identified through its high content of Ti atoms (green dots). Within the primary precipitate, secondary Fe-rich precipitates (A2*) were found.

Song et al. [9] reported that in their alloy with 4.4 at.% Ti, Fe is enriched on APBs within the $L2_1$ precipitates during aging at 700 °C due to a phase separation, i.e., $L2_1 \rightarrow$ Fe-rich $A2 + L2_1$. Allen et al. [40] reported for the B2–NiAl phase that disordered Fe inclusions arise through either homogeneous nucleation within the ordered domains or heterogeneous nucleation at APBs. In the alloy investigated in the present work, both formation processes were observed. Song et al. [9] showed that, after aging at 700 °C, additional $L2_1$ secondary precipitates are present within the matrix that are formed during the cooling process. In the present study, however, no secondary precipitates were found within the matrix.

The formation of a subprecipitate structure composed of near A2 composition within the primary precipitates was also observed in B2–NiAl-containing alloys [41] and, on a much larger scale, in $L2_1$-strengthened ferritic alloys [20]. The B2 and $L2_1$ phases are supersaturated with Fe, which is in agreement with the solubility ranges of NiAl–FeAl and $Ni_2TiAl–Fe_2TiAl$ as was consistently reported by [17,22,41,42]. The formation of secondary disordered γ precipitates is also observed in the γ' phase of Ni-based superalloys and can contribute to a further hardening of the alloys [43,44]. Baik et al. [21] suggested that this might also happen in their Fe–Ni–Al–Cr–Ti alloy. Such behavior is expected to prevent the deterioration of the microstructure during aging at high temperatures.

The phase fraction of the precipitates can be determined by applying the lever rule given in Equation (1) [45,46]:

$$f_{L2_1} = \frac{C_{bulk} - C_{matrix}}{C_{precipitate} - C_{matrix}} \tag{1}$$

where C_{bulk} is the global composition of the alloy, which is given in Table 1; and C_{matrix} and $C_{precipitate}$ are the chemical compositions of the A2 matrix and $L2_1$ precipitate, respectively. The numerator and the denominator were calculated for each alloying element (Fe, Al, Ni, Ti). Because the alloy comprises two phases, the slope of the linear fit represents the mole fraction of the $L2_1$ precipitates. The determined phase fraction of the precipitates in the water-quenched condition is 58.7 vol. %; in the furnace-cooled state, it was lower, with 52.8 vol. %.

The phase compositions of the water-quenched and furnace-cooled states are summarized in Table 3. Standard deviation is ±0.1 at.%. In both conditions, the matrix mainly consisted of Fe and dissolved about 13 at. % Al, and up to 1 at. % Ni and Ti, respectively. The primary precipitates were identified as off-stoichiometric $L2_1$-$(Fe,Ni)_2TiAl$ precipitates.

Table 3. Quantitative analysis of the phase compositions in at. % of water-quenched (WQ) or furnace-cooled (FC) samples from 1200 °C obtained from APT measurements in voltage mode (see text). Standard deviation is ±0.1 at.%. The water-quenched sample was composed of the A2 matrix phase and primary $L2_1$ precipitates; in the furnace-cooled state, secondary Fe-rich precipitates (A2*) were also found within the primary $L2_1$ precipitates.

Sample	Phase	Fe (at. %)	Al (at. %)	Ni (at. %)	Ti (at. %)	Other (at. %)
WQ	A2	84.5	12.9	1.1	1.1	0.4
	L21	41.3	24.7	17.0	16.5	0.5
FC	A2	85.4	12.9	0.8	0.6	0.3
	L21	36.4	26.3	18.5	18.3	0.5
	A2*	79.1	13.3	4.3	3.3	0.0

In the furnace-cooled state, the secondary precipitates within the primary $L2_1$ precipitates show a slightly different chemical composition than that of the A2 matrix. They contained about 6 at. % less Fe, but considerably more Ni and Ti compared to the matrix. However, the measured Al content is similar. It was assumed that these secondary precipitates could also be related to the disordered A2 phase. The secondary precipitates are denoted as A2* to emphasize that they had a different chemical composition than that of the A2 matrix itself.

3.4. Long-Term Annealing

Figure 10 shows the microstructures after long-term annealing at 900 °C for 100 h and following water quenching (Figure 10a) or furnace cooling (Figure 10b). The $L2_1$ precipitates coarsened substantially during annealing at 900 °C in the A2 + $L2_1$ two-phase region. After cooling to room temperature, precipitates in the furnace-cooled condition were slightly larger than those in the water-quenched condition. This is in line with the observations on the samples furnace-cooled or quenched from 1200 °C and is related to the shift of the A2 + $L2_1$ phase boundary with decreasing temperature. While in the quenched sample, the compositions of the phases attained at 900 °C are preserved to room temperature, the shift of the phase boundary with decreasing temperature even below 900 °C leads to a shift in compositions and thereby of the phase fractions if the samples are slowly cooled. The precipitate sizes increased by a factor of 10 to 20 (longitudinal axis 1 to 10 μm) after annealing for 100 h when compared to the sample which were homogenized in the A2 single-phase field region at 1200 °C and subsequent furnace cooling. The morphology of the precipitates also changed from spherical to rectangular, and regions could be identified where coalesced particles were forming rod-shaped features.
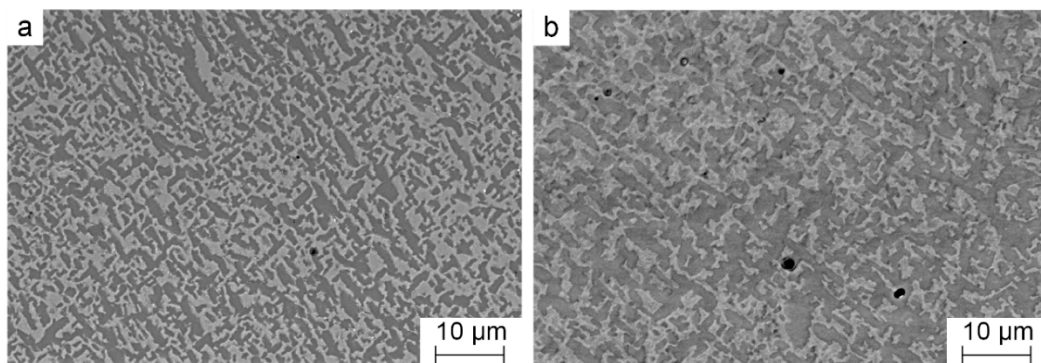
Figure 10. SEM images taken in BSE mode of the microstructures after heat treatment at 900 °C for 100 h followed by (**a**) water quenching or (**b**) furnace cooling.

This behavior might have been because of the loss of coherency of the precipitates. Doi et al. [47] reported that, with an increasing degree of lattice mismatch, precipitates change from spheres into cuboids, and further into needles or plates. Changes in morphology and coarsening during long-term annealing can be retarded by optimizing the lattice mismatch between matrix and precipitates [39,47]. Through adjusting the composition of the alloy or by the addition of further alloying elements, the lattice mismatch of the matrix–precipitate interface can be optimized, so that these interfaces become coherent instead of being semicoherent. Baik et al. [21] suggested that secondary disordered precipitates that have the same composition and crystal structure as those of the matrix phase could split the primary ordered precipitates and thus prevent the degradation of the microstructure (see Section 3.3). In the investigated alloy, however, there was no evidence of the split of the primary precipitates after long-term annealing at 900 °C.

3.5. Hardness Measurements

Hardness measurements (HV10) were performed on samples in as-cast and heat-treated states. The arithmetic means of five indents are given in Table 4. In the as-cast condition and after thermal exposure at 1200 °C, followed by water quenching, high hardness values (608 and 699 HV10, respectively) were achieved; after furnace cooling, the resulting hardness value (463 HV10) was significantly lower. The increased hardness was caused by different strengthening mechanisms that are discussed below.

Table 4. Arithmetic means and standard deviation of hardness values according to HV10 of samples in the as-cast state and after heat treatment at 1200 °C for 24 h or at 900 °C for 100 h followed by either water quenching (WQ) or furnace cooling (FC).

State	As-Cast	1200 °C-WQ	1200 °C-FC	900 °C-WQ	900 °C-FC
HV10	608 ± 7	699 ± 8	463 ± 4	447 ± 6	446 ± 4

In both samples that were quickly cooled to room temperature (as-cast and water-quenched), submicron precipitates were present, because the samples were quenched from above the dissolution temperature of the $L2_1$ phase. In the as-cast state, the measured hardness value was about 90 HV10 lower than that after water quenching because of the slightly lower cooling rate of the casting process due to the larger sample mass. The high volume fraction of precipitates <100 nm that was present in the rapidly cooled samples was responsible for the increased hardness. In contrast to the as-cast and water-quenched condition, after furnace cooling, the precipitates were coarser, with precipitate sizes of about 300–700 nm, resulting in decreased hardness. Another factor that affects increased hardness after water quenching is the higher level of thermal stresses within the samples. In FeAl- and Fe_3Al-based alloys, the content of quenched-in vacancies and APBs hugely impacts

the strength of the materials [48,49]. Depending on the heat treatment and Al-content of the alloys, up to a few at. % of quenched-in vacancies may be present at room temperature.

According to [48–50], excess vacancies significantly contribute to hardening because they impede dislocation motion. The investigated alloys are additionally strengthened by APBs, which also act as obstacles to dislocation motion. Hasemann et al. [51] described that, especially in Fe-rich alloy compositions, APBs are more effective in strengthening because in such alloys, the concentration of quenched-in vacancies is comparatively small.

After long-term annealing at 900 °C for 100 h followed by either water quenching or furnace cooling. precipitates are even coarser, with precipitate sizes of 1–10 μm. This is reflected in lower hardness values of about 445 HV10 in both states. After cooling from 900 °C, thermal vacancies and thermal stresses appeared to impact the alloys' hardness less. The hardness may mainly be influenced by the microstructure itself, resulting in similar hardness values after water quenching and furnace cooling.

4. Conclusions

In this study, the microstructure of a precipitation-strengthened ferritic alloy with a nominal composition of 60Fe–20Al–10Ni–10Ti (in at. %) was examined by employing SEM, TEM, APT, DTA, and XRD. In contrast to previously investigated Fe–Al–Cr–Ni–Ti(–Mo) alloys [8,9,17–20], Cr and Mo were omitted in order to reduce the alloy's density. Considering all investigations, the following conclusions can be drawn:

- Within the Fe–Al–Ni–Ti system, microstructures can be generated that comprise a disordered ferritic matrix (A2 structure) and intermetallic Heusler precipitates ($L2_1$ structure).
- Alloying with Ti increases the dissolution temperature of the $L2_1$ phase when compared to the stoichiometric binary $D0_3$ phase. In the investigated alloy, the $L2_1$ precipitates were stable at least up to 920 °C, which is an indispensable requirement for applying the alloy at high temperatures.
- After water quenching from 1200 °C, i.e., from the A2 single-phase field region, the microstructure was built up of two phases, A2 and $L2_1$. Their arrangement resembled the γ/γ' microstructure of Ni-based superalloys. APT measurements revealed that the A2 matrix was continuous, and cuboidal $L2_1$ precipitates were embedded in the matrix. After furnace cooling, the A2 matrix was still continuous. However, the $L2_1$ precipitates became spherical and were coarser than those in the water-quenched state.
- TEM showed that the matrix–precipitate interface was coherent in the water-quenched state, which was a consequence of a sufficiently small lattice mismatch. After furnace cooling, the mismatch was larger, resulting in semicoherent interfaces. After long-term annealing at 900 °C in the A2 + $L2_1$ region for 100 h, the precipitates substantially coarsened.
- APT investigations revealed that, after furnace cooling from 1200 °C, secondary Fe-rich precipitates are present within the primary $L2_1$ precipitates. The phase compositions suggest that these particles could be ascribed to the A2 phase. These secondary precipitates are either formed on antiphase boundaries by heterogeneous nucleation or in the center of the $L2_1$ precipitates by homogeneous nucleation. In all investigated states, the $L2_1$ phase was identified as off-stoichiometric $(Fe,Ni)_2TiAl$, with Fe being its major constituent.

Author Contributions: Conceptualization, F.G., M.P. and H.C.; investigation, F.G., C.H.L., F.S., C.T., K.L. and B.R.; data curation, F.G.; writing—original draft preparation, F.G.; writing—review and editing, M.P., H.C., F.S., C.H.L. and B.R.; supervision, F.G., M.P. and H.C.; project administration, F.G. and H.C. All authors have read and agreed to the published version of the manuscript.

References

1. Stallybrass, C.; Sauthoff, G. Ferritic Fe-Al-Ni-Cr alloys with coherent precipitates for high-temperature applications. *Mater. Sci. Eng. A* **2004**, *387–389*, 985–990. [CrossRef]
2. Stallybrass, C.; Schneider, A.; Sauthoff, G. The strengthening effect of (Ni,Fe)Al precipitates on the mechanical properties at high temperatures of ferritic Fe-Al-Ni-Cr alloys. *Intermetallics* **2005**, *13*, 1263–1268. [CrossRef]
3. Teng, Z.K.; Liu, C.T.; Miller, M.K.; Ghosh, G.; Kenik, E.A.; Huang, S.; Liaw, P.K. Room temperature ductility of NiAl-strengthened ferritic steels: Effects of precipitate microstructure. *Mater. Sci. Eng. A* **2012**, *541*, 22–27. [CrossRef]
4. Teng, Z.K.; Zhang, F.; Miller, M.K.; Liu, C.T.; Huang, S.; Chou, Y.T.; Tien, R.H.; Chang, Y.A.; Liaw, P.K. New NiAl-strengthened ferritic steels with balanced creep resistance and ductility designed by coupling thermodynamic calculations with focused experiments. *Intermetallics* **2012**, *29*, 110–115. [CrossRef]
5. Sun, Z.; Liebscher, C.H.; Huang, S.; Teng, Z.; Song, G.; Wang, G.; Asta, M.; Rawlings, M.; Fine, M.E.; Liaw, P.K. New design aspects of creep-resistant NiAl-strengthened ferritic alloys. *Scr. Mater.* **2013**, *68*, 384–388. [CrossRef]
6. Vo, N.Q.; Liebscher, C.H.; Rawlings, M.J.S.; Asta, M.; Dunand, D.C. Creep properties and microstructure of a precipitation-strengthened ferritic Fe-Al-Ni-Cr alloy. *Acta Mater.* **2014**, *71*, 89–99. [CrossRef]
7. Huang, S.; Gao, Y.; An, K.; Zheng, L.; Wu, W.; Teng, Z.; Liaw, P.K. Deformation mechanisms in a precipitation-strengthened ferritic superalloy revealed by in situ neutron diffraction studies at elevated temperatures. *Acta Mater.* **2015**, *83*, 137–148. [CrossRef]
8. Liebscher, C.H.; Radmilovic, V.; Dahmen, U.; Asta, M.; Ghosh, G. On the formation of hierarchically structured $L2_1$-Ni_2TiAl type precipitates in a ferritic alloy. *J. Mater. Sci.* **2013**, *48*, 2067–2075. [CrossRef]
9. Song, G.; Sun, Z.; Poplawsky, J.; Gao, Y.; Liaw, P.K. Microstructural evolution of single Ni_2TiAl or hierarchical $NiAl/Ni_2TiAl$ precipitates in Fe-Ni-Al-Cr-Ti ferritic alloys during thermal treatment for elevated-temperature applications. *Acta Mater.* **2017**, *127*, 1–16. [CrossRef]
10. Strutt, P.R.; Polvani, R.S.; Ingram, J.C. Creep behavior of the Heusler type structure alloy Ni_2AlTi. *Metall. Trans. A* **1976**, *7*, 23–31. [CrossRef]
11. Pearson, W.B.; Raynor, G.V. *Handbook of Lattice Spacings and Structure of Metals*; Pergamon Press: Oxford, UK, 1958. [CrossRef]
12. Jung, J.; Ghosh, G.; Olson, G.B. A comparative study of precipitation behavior of Heusler phase (Ni_2TiAl) from B2-TiNi in Ni-Ti-Al and Ni-Ti-Al-X (X = Hf, Pd, Pt, Zr) alloys. *Acta Mater.* **2003**, *51*, 6341–6357. [CrossRef]
13. Nachman, J.F.; Buehler, W.J. Fe-Al-Mo alloys for high-temperature use. *Met. Prog.* **1956**, *70*, 107–110.
14. Bordeau, R.G. *Development of Iron Aluminides*; Air Force Wright Aeronautical Laboratories Report AFWAL-TR-87-4009; Wright-Patterson Air Force Base: Dayton, OH, USA, 1987; pp. 1–263.
15. Judkins, R.R.; Rao, U.S. Fossil energy applications of intermetallic alloys. *Intermetallics* **2000**, *8*, 1347–1354. [CrossRef]
16. Morris, D.G.; Munoz-Morris, M.A. Recent developments toward the application of iron aluminides in fossil fuel technologies. *Adv. Eng. Mater.* **2011**, *13*, 43–47. [CrossRef]
17. Liebscher, C.H.; Radmilovic, V.R.; Dahmen, U.; Vo, N.Q.; Dunand, D.C.; Asta, M.; Ghosh, G. A hierarchical microstructure due to chemical ordering in the bcc lattice: Early stages of formation in a ferritic Fe-Al-Cr-Ni-Ti alloy. *Acta Mater.* **2015**, *92*, 220–232. [CrossRef]
18. Song, G.; Sun, Z.; Li, L.; Xu, X.; Rawlings, M.; Liebscher, C.H.; Clausen, B.; Poplawsky, J.; Leonard, D.N.; Huang, S.; et al. Ferritic alloys with extreme creep resistance via coherent hierarchical precipitates. *Sci. Rep.* **2015**, *5*, 16327. [CrossRef] [PubMed]
19. Song, G.; Sun, Z.; Clausen, B.; Liaw, P.K. Microstructural characteristics of a Ni_2TiAl-precipitate-strengthened ferritic alloy. *J. Alloys Compd.* **2017**, *693*, 921–928. [CrossRef]
20. Rawlings, M.J.S.; Liebscher, C.H.; Dunand, D.C. Effect of titanium additions upon structure and properties of precipitation-strengthened Fe-Al-Ni-Cr-Ti ferritic alloys. *Acta Mater.* **2017**, *128*, 103–112. [CrossRef]
21. Baik, S.; Rawlings, M.J.S.; Dunand, D.C. Atom probe tomography study of Fe-Ni-Al-Cr-Ti ferritic steels with hierarchically-structured precipitates. *Acta Mater.* **2018**, *144*, 707–715. [CrossRef]
22. Li, C.; Ma, Y.; Hao, J.; Yan, Y.; Wang, Q.; Dong, C.; Liaw, P.K. Microstructures and mechanical properties of body-centered-cubic $(Al,Ti)_{0.7}(Ni,Co,Fe,Cr)_5$ high entropy alloys with coherent $B2/L2_1$ nanoprecipitation. *Mater. Sci. Eng. A* **2018**, *737*, 286–296. [CrossRef]
23. Baik, S.; Wang, S.Y.; Liaw, P.K.; Dunand, D.C. Increasing the creep resistance of Fe-Ni-Al-Cr superalloys via Ti additions by optimizing the B2/L21 ratio in composite nano-precipitates. *Acta Mater.* **2018**, *157*, 142–154. [CrossRef]
24. Stepanov, N.D.; Shaysultanov, D.G.; Tikhonovsky, M.A.; Zherebtsov, S.V. Structure and high temperature mechanical properties of novel non-equiatomic Fe-(Co, Mn)-Cr-Ni-Al-(Ti) high entropy alloys. *Intermetallics* **2018**, *102*, 140–151. [CrossRef]
25. Wolff-Goodrich, S.; Marshal, A.; Pradeep, K.G.; Dehm, G.; Schneider, J.M.; Liebscher, C.H. Combinatorial exploration of $B2/L2_1$ precipitation strengthened AlCrFeNiTi compositionally complex alloys. *J. Alloys Compd.* **2021**, *853*, 156111. [CrossRef]
26. Kim, W.C.; Na, M.Y.; Kwon, H.J.; Na, Y.S.; Jong, W.W.; Chang, H.J.; Lim, K.R. Designing $L2_1$-strengthened Al-Cr-Fe-Ni-Ti complex concentrated alloys for high temperature applications. *Acta Mater.* **2021**, *211*, 116890. [CrossRef]

27. Wolff-Goodrich, S.; Haas, S.; Glatzel, U.; Liebscher, C.H. Towards superior high temperature properties in low density ferritic AlCrFeNiTi compositionally complex alloys. *Acta Mater.* **2021**, *216*, 117113. [CrossRef]

28. Yan, X.; Grytsiv, A.; Rogl, P.; Pomjakushin, V.; Palm, M. The Heusler phase $Ti_{25}(Fe_{50-X}Ni_x)Al_{25}$ (0<x<50); Structure and constitution. *J. Phase Equilibria Diffus.* **2008**, *29*, 500–508. [CrossRef]

29. Krein, R.; Palm, M.; Heilmaier, M. Characterization of microstructures, mechanical properties, and oxidation behavior of coherent A2 + $L2_1$ Fe-Al-Ti. *J. Mater. Res.* **2009**, *24*, 3412–3421. [CrossRef]

30. Lawley, A.; Cahn, R.W. A high temperature X-ray study of ordering in iron-aluminium alloys. *J. Phys. Chem. Solids* **1961**, *20*, 204–221. [CrossRef]

31. Lee, J.C.; Su, D.; Chuang, J.H. A novel application of the FIB lift-out technique for 3-D TEM analysis. *Microelectron. Reliab.* **2001**, *41*, 1551–1556. [CrossRef]

32. Thompson, K.; Lawrence, D.; Larson, D.J.; Olson, J.D.; Kelly, T.F.; Gorman, B. In situ site-specific specimen preparation for atom probe tomography. *Ultramicroscopy* **2007**, *107*, 131–139. [CrossRef]

33. Ohnuma, I.; Schön, G.; Kainuma, R.; Inden, G.; Ishida, K. Ordering and phase separation in the b.c.c. phase of the Fe-Al-Ti system. *Acta Mater.* **1998**, *46*, 2083–2094. [CrossRef]

34. Eleno, L.T.F.; Errico, L.A.; Gonzales-Ormeño, P.G.; Petrilli, H.M.; Schön, C.G. Ordering phase relationships in ternary iron aluminides. *Calphad* **2014**, *44*, 70–80. [CrossRef]

35. Mazauric, V.; Finel, A.; Ducastelle, F. Theoretical study of antiphase boundaries in fcc alloys: Wetting and layering effects. *Phase Transit.* **1991**, *30*, 233–242. [CrossRef]

36. Murakami, Y.; Yanagisawa, K.; Niitsu, K.; Park, H.S.; Matsuda, T.; Kainuma, R.; Shindo, D.; Tonomura, A. Determination of magnetic flux density at the nanometer-scale antiphase boundary in Heusler alloy $Ni_{50}Mn_{25}Al_{12.5}Ga_{12.5}$. *Acta Mater.* **2013**, *61*, 2095–2101. [CrossRef]

37. Bendersky, L.A.; Voorhees, P.W.; Boettinger, W.J.; Johnson, W.C. The role of elastic energy in the morphological development of a Ni-Ti-Al alloy. *Scr. Metall.* **1988**, *22*, 1029–1034. [CrossRef]

38. Su, C.H.; Voorhees, P.W. The dynamics of precipitate evolution in elastically stressed solids—II. Particle alignment. *Acta Mater.* **1996**, *44*, 2001–2016. [CrossRef]

39. Johnson, W.C.; Voorhees, P.W. Elastic interaction and stability of misfitting cuboidal inhomogeneities. *J. Appl. Phys.* **1987**, *61*, 1610–1619. [CrossRef]

40. Allen, S.M.; Cahn, J.W. Mechanisms of phase transformations within the miscibility gap of Fe-rich Fe-Al alloys. *Acta Metall.* **1976**, *24*, 425–437. [CrossRef]

41. Teng, Z.K.; Miller, M.K.; Ghosh, G.; Liu, C.T.; Huang, S.; Russell, K.F.; Fine, M.E.; Liaw, P.K. Characterization of nanoscale NiAl-type precipitates in a ferritic steel by electron microscopy and atom probe tomography. *Scr. Mater.* **2010**, *63*, 61–64. [CrossRef]

42. Kainuma, R.; Urushiyama, K.; Ishikawa, K.; Jia, C.C.; Ohnuma, I.; Ishida, K. Ordering and phase separation in b.c.c. aluminides of the Ni–Fe–Al–Ti system. *Mater. Sci. Eng. A* **1997**, *239–240*, 235–244. [CrossRef]

43. Doi, M.; Miki, D.; Moritani, T.; Kozakai, T. Gamma/gamma-prime microstructure formed by phase sepearation of gamma-prime precipitates in a Ni-Al-Ti alloy. In *Superalloys 2004*; Green, K.A., Pollock, T.M., Harada, H., Howson, T.E., Reed, R.C., Schirra, J.J., Walston, S., Eds.; TMS: Seven Springs, PA, USA, 2004; pp. 109–114.

44. Vogel, F.; Wanderka, N.; Balogh, Z.; Ibrahim, M.; Stender, P.; Schmitz, G.; Banhart, J. Mapping the evolution of hierarchical microstructures in a Ni-based superalloy. *Nat. Commun.* **2013**, *4*, 2955. [CrossRef] [PubMed]

45. Miller, M.K.; Forbes, R.G. *Atom-Probe Tomography: The Local Electrode Atom Probe*; Springer: New York, NY, USA, 2014. [CrossRef]

46. Blavette, D.; Cadel, E.; Deconihout, B. Role of the atom probe in the study of nickel-based superalloys. *Mater. Charact.* **2000**, *44*, 133–157. [CrossRef]

47. Doi, M.; Miyazaki, T. The effect of elastic interaction energy on the morphology of γ' precipitates in Nickel-based alloys. *Mater. Sci. Eng.* **1984**, *67*, 247–253. [CrossRef]

48. Leamy, H.J.; Kayser, F.X. The compressive deformation behavior of long range ordered polycrystalline iron-aluminum alloys. *Phys. Status Solidi* **1969**, *34*, 765–780. [CrossRef]

49. Hasemann, G.; Schneibel, J.H.; Krüger, M.; George, E.P. Vacancy strengthening in Fe_3Al iron aluminides. *Intermetallics* **2014**, *54*, 95–103. [CrossRef]

50. Herrmann, J.; Inden, G.; Sauthoff, G. Deformation behaviour of iron-rich iron-aluminum alloys at low temperatures. *Acta Mater.* **2003**, *51*, 2847–2857. [CrossRef]

51. Hasemann, G.; Schneibel, J.H.; George, E.P. Dependence of the yield stress of Fe_3Al on heat treatment. *Intermetallics* **2012**, *21*, 56–61. [CrossRef]